Journal of Solid State Chemistry 181 (2008) 2672–2680

Contents lists available at ScienceDirect

Journal of Solid State Chemistry

journal homepage: www.elsevier.com/locate/jssc

Hydrothermal synthesis and luminescent properties of $LuBO_3$:Tb^{3+} microflowers

Jun Yang [a,b], Cuimiao Zhang [a,b], Lili Wang [a,b], Zhiyao Hou [a,b], Shanshan Huang [a,b], Hongzhou Lian [a,b], Jun Lin [a,b,*]

[a] State Key Laboratory of Rare Earth Resource Utilization, Changchun Institute of Applied Chemistry, Chinese Academy of Sciences, Changchun, Jilin 130022, PR China
[b] Graduate University of the Chinese Academy of Sciences, Beijing 100049, PR China

ARTICLE INFO

Article history:
Received 8 May 2008
Received in revised form
19 June 2008
Accepted 20 June 2008
Available online 27 June 2008

Keywords:
Hydrothermal synthesis
$LuBO_3$
Terbium
Luminescence
Green phosphor

ABSTRACT

Hexagonal vaterite-type $LuBO_3$:Tb^{3+} microflower-like phosphors have been successfully prepared by an efficient surfactant- and template-free hydrothermal process directly without further sintering treatment. X-ray diffraction (XRD), Fourier transform infrared spectroscopy (FT-IR), thermogravimetric analysis (TGA), scanning electron microscopy (SEM), energy-dispersive X-ray (EDX) spectrometry, transmission electron microscopy (TEM), high-resolution transmission electron microscopy (HRTEM), selected area electron diffraction (SAED), photoluminescence (PL) and cathodoluminescence (CL) spectra as well as kinetic decays were used to characterize the samples. The as-obtained phosphor samples present flowerlike agglomerates composed of nanoflakes with thickness of 40 nm and high crystallinity in spite of the moderate reaction temperature of 200 °C. The reaction mechanism has been considered as a dissolution/precipitation mechanism; the self-assembly evolution process has been proposed on homocentric layer-by-layer growth style. Under ultraviolet excitation into the $4f^8 \rightarrow 4f^7 5d$ transition of Tb^{3+} at 248 nm (or 288 nm) and low-voltage electron beam excitation, $LuBO_3$:Tb^{3+} samples show the characteristic green emission of Tb^{3+} corresponding to $^5D_4 \rightarrow {}^7F_{6,5,4,3}$ transitions with the $^5D_4 \rightarrow {}^7F_5$ transition (542 nm) being the most prominent group, which have potential applications in fluorescent lamps and field emission displays.

1. Introduction

To obtain desired rare earth (RE) ions doped phosphors, wet chemistry processes, such as co-precipitation [1a], hydrothermal synthesis [1b,c], and colloidal chemistry [1d], are extensively used because starting materials in these methods can be mixed at the molecular level and the reaction temperature for forming the desired products is relatively low. However, most phosphors prepared from wet chemistry methods crystallize and exhibit luminescence only after being sintered at high temperature. This is because OH^- groups and/or crystal water molecules attached on the particle surface or in the host lattice are unavoidable and may quench the luminescence. Consequently, further sintering these precursors at higher temperature is needed to improve the luminescence intensity in most cases [2]. But, this cannot work for those phosphors based on Tb^{3+} ions, which will be oxidated easily at higher temperature in the atmosphere.

It is well known that phosphors based on orthoborates have attracted much attention due to their high stability, low synthetic temperature, and high ultraviolet and optical damage threshold [3]. Rare earth orthoborates $LnBO_3$ (Ln = lanthanides and yttrium) have proved to be very useful host lattices for the luminescence of Eu^{3+} and Tb^{3+}, which have found wide applications in Hg-free fluorescent lamps and in various kinds of display devices [4]. For example, YBO_3:Eu^{3+}/Tb^{3+} are currently used as a red/green component in PDP television. Remarkably, lutetium (Lu) may be a more favorable cation than yttrium (Y) for trivalent lanthanide dopant emission due to the intensity-borrowing mechanism mixing the 4*f* and 5*d* orbitals of the Ln^{3+} ion via the lattice valence band levels [5]. Lutetium orthoborates ($LuBO_3$), due to its high density and high damage threshold, have been considered as a promising host matrix for RE ions substitution to produce phosphors, lasers or scintillators [6]. In fact, conventional solid-state reaction and sol–gel process-derived $LuBO_3$:Eu^{3+}/Tb^{3+} phosphors have bad irregular shapes and agglomerated particles [7] due to the high annealing temperature and repeat grinding process, which will limit its

* Corresponding author at: State Key Laboratory of Rare Earth Resource Utilization, Changchun Institute of Applied Chemistry, Chinese Academy of Sciences, 5625 Renmin Street, Changchun, Jilin 130022, PR China.
Fax: +86 431 85698041.
E-mail address: jlin@ciac.jl.cn (J. Lin).

0022-4596/$ - see front matter © 2008 Elsevier Inc. All rights reserved.
doi:10.1016/j.jssc.2008.06.045

dispersing stability and subsequent coating ability on the display panels [4d]. Accordingly, $LuBO_3:Eu^{3+}/Tb^{3+}$ phosphors with homogeneous, monodispersed and well-defined morphology are highly desired. It is well known that the hydrothermal method is a promising synthetic route, which can be better controlled from the molecular precursor to the reaction parameters, such as the reaction time and temperature, to give highly pure and homogeneous materials. The technique allows low reaction temperature and controllable size, phase and morphology of the products [8]. Although there have been some reports about the hydrothermal/solvothermal synthesis and properties of rare earth orthoborate materials, all of them were focused on YBO_3, $GdBO_3$ and $NdBO_3$ [9]. To the best of our knowledge, few studies about hydrothermal/solvothermal synthesis of $LuBO_3(:Tb^{3+})$ have been reported [1c].

Herein we report an efficient surfactant- and template-free hydrothermal approach to synthesize hexagonal $LuBO_3:Tb^{3+}$ with novel self-assembled 3D architectures. These microflowers, which were composed of nanosized units, were expected to maintain the desirable properties of $LuBO_3:Tb^{3+}$ nanocrystals (flakes) while being quite stable on the micrometer scale. In spite of the moderate reaction temperature of 200 °C, the as-synthesized $LuBO_3:Tb^{3+}$ is highly crystalline. The luminescent properties of the flowerlike $LuBO_3:Tb^{3+}$ composed of nanoflakes have also been reported and investigated in detail in comparison with the products directly obtained from conventional solid-state reaction, which shows it is a good green-emitting phosphor.

2. Experimental section

2.1. Materials

The initial chemicals in this work, Lu_2O_3 and Tb_4O_7 (both with purity of 99.99%, Changchun Applied Chemistry Science and Technology Limited, China), HCl, H_3BO_3, $NH_3 \cdot H_2O$ and ethanol (all with purity of A.R., Beijing Fine Chemical Company, China), were used without further purification.

2.2. Preparation

Firstly, Lu_2O_3 and Tb_4O_7 were dissolved in dilute HCl, resulting in the formation of a colorless stock solution of $LuCl_3$ with 0.2 mol L^{-1} and a colorless solution of $TbCl_3$ with 0.02 and 0.2 mol L^{-1}. In a typical hydrothermal synthesis, stoichiometric amounts of $LuCl_3$ solution, $TbCl_3$ solution (Lu:Tb = 99:1, 95:5, 90:10, 85:15, 80:20, in molar ratio) and H_3BO_3 (100% excess) were mixed under stirring, then deionized water was added to the above mixture to reach 41 mL for total volume of H_2O solution. The solution was stirred for another 30 min to form a clear aqueous solution. Then 25 wt% of $NH_3 \cdot H_2O$ (A.R.) was introduced dropwise to the vigorously stirred solution until pH = 7. After additional agitation for 40 min, the as-obtained white colloidal precipitate was transferred to a 50 mL autoclave, sealed, and heated at 200 °C for 24 h. It was then cooled to room temperature naturally. The products were then collected by filtration, washed with ethanol and deioned water for several times, and dried in atmosphere at 100 °C for 6 h. For comparison, the same Tb^{3+} content bulk $LuBO_3:Tb^{3+}$ phosphors were also synthesized by normal direct solid-state reaction (SR) using stoichiometric amounts of Lu_2O_3, Tb_4O_7 (Lu:Tb = 85:15, in molar ratio) and H_3BO_3 (50% excess) at 1300 °C for 2 h in a reducing atmosphere of CO.

2.3. Characterization

The phase purity and crystallinity of the samples were examined by powder X-ray diffraction (XRD) performed on a Rigaku-Dmax 2500 diffractometer with Cu$K\alpha$ radiation ($\lambda = 0.15405$ nm). Fourier transform infrared spectroscopy (FT-IR) spectra were measured with a Perking-Elmer 580B infrared spectrophotometer with the KBr pellet technique. Thermogravimetric analysis (TGA) data were recorded with a Thermal Analysis Instrument (SDT 2960, TA Instruments, New Castle, DE) with a heating rate of 10 °C min^{-1} in an N_2 flow of 100 mL min^{-1}. The morphology and structure of the samples were inspected using a field emission scanning electron microscopy equipped with an energy-dispersive X-ray (EDX) spectrometer (FE-SEM, XL 30, Philips) and a transmission electron microscope. Low-resolution transmission electron microscopy (TEM) images and selective area electron diffraction (SAED) patterns were obtained using a JEOL 2010 transmission electron microscope operating at 150 kV. High-resolution transmission electron microscopy (HRTEM) images were performed using FEI Tecnai G2 S-Twinwere with a field emission gun operating at 200 kV. Images were acquired digitally on a Gatan multiple CCD camera. Photoluminescence (PL) excitation and emission spectra were recorded with a Hitachi F-4500 spectrophotometer equipped with a 150 W Xenon lamp as the excitation source at room temperature. The cathodoluminescent (CL) measurements were carried out in an ultra-high-vacuum chamber ($<10^{-8}$ Torr), where the samples were excited by an electron beam at a voltage range of 1–5 kV with different filament currents, and the spectra were recorded on an F-4500 spectrophotometer. The luminescence decay curves were obtained from a Lecroy Wave Runner 6100 Digital Osilloscope (1 GHz) using a tunable laser (pulse width = 4 ns, gate = 50 ns) as the excitation (Contimuum Sunlite OPO). All measurements were performed at room temperature (RT).

3. Results and discussion

3.1. Phase formation

Fig. 1a shows the XRD pattern of the as-formed $LuBO_3$:15%Tb^{3+} flowerlike products through the hydrothermal process. All diffraction peaks can be readily indexed to a pure hexagonal phase of $LuBO_3$ crystal [space group: $P63/mmc(194)$] with

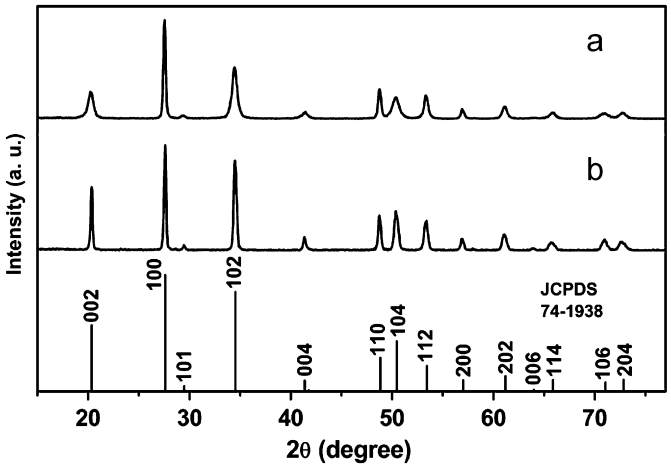

Fig. 1. XRD patterns for the $LuBO_3$:15%Tb^{3+} sample obtained from the hydrothermal process (a) and solid-state reaction (b), respectively. The standard data for hexagonal vaterite-type $LuBO_3$ (JCPDS card 74-1938) are also presented for comparison.

vaterite-type structure (JCPDS 74-1938). No additional peaks of other phases have been found, indicating that Tb^{3+} has been effectively built into the host lattice. The calculated lattice constants, $a = b = 3.733$ Å, $c = 8.736$ Å is well compatible with the literature values of $a = b = 3.727$ Å, $c = 8.722$ Å (JCPDS 74-1938). Moreover, high crystallinity can be obtained at a relatively low temperature. This is important for phosphors, since high crystallinity always means less traps and stronger luminescence. The *Ln* orthoborates, $LnBO_3$, have been known to possess the three polymorphic forms of $CaCO_3$: aragonite, vaterite and calcite [7c]. There exists, however, no individual $LnBO_3$ with all three polymorphs. $LuBO_3$ synthesized by means of a solid-state reaction method presents both a low-temperature calcite form ($<1300\,^{\circ}C$) and a high-temperature vaterite form ($>1300\,^{\circ}C$) [10a]. In our present process, we obtained vaterite form $LuBO_3$ at a low temperature of 200 °C, much lower than the synthesis temperature of traditional solid-state reaction (SR). This is just one of the merits in the current hydrothermal process, like the sol–gel process to prepare $LuBO_3$ with a vaterite form at relative low temperatures [10b].

Although all peaks of the as-formed $LuBO_3$:15%Tb^{3+} flowerlike products through the hydrothermal process can be assigned exactly to the standard data of $LuBO_3$ (JCPDS 74-1938), some of its peaks display quite distinct broadening behavior compared with those of the bulk sample synthesized through a solid-state reaction (SR) (Fig. 1b). Specifically, the (002), (102), (004) and (104) peaks are much broader than those of the SR sample, which is accompanied by an appreciable decrease in their intensity. In addition, the (002) peak is much broader than the (100) peak in the hydrothermal sample, which is the characteristic of two-dimensional nanomaterials [9a]. These results imply that the hydrothermal products are presumably nanosheets. Further FE-SEM characterization of this sample (see below, Fig. 3) shows that they grow preferentially along the (001) direction, resulting in the formation of nanoflakes. According to the broadening behavior of the XRD peaks, the nanoflake thickness can be estimated from the Scherrer equation

$$D = 0.941\lambda/\beta \cos\theta \quad (1)$$

where D is the average grain size, λ the X-ray wavelength (0.15405 nm), and θ and β the diffraction angle and full-width at half-maximum (fwhm, in radian) of an observed peak, respectively [10c]. These peaks at $2\theta = 27.504^{\circ}$ and 56.900° are assigned to the (100) and (200) crystallographic planes, respectively, and they are perpendicular to the (001) plane and are used to calculate the nanoflake thickness with an average value of 26.6 nm.

Fig. 2a shows the IR spectrum of the $LuBO_3$:15%Tb^{3+} sample. The vibrational spectra of vaterite-type borates are found to be markedly different from those of calcite and aragonite-type borates. There is a group of bands in the region 800–1200 cm^{-1} in vaterite-type borates. The IR spectrum of our present sample was in accordance with Ref. [10d]. Accordingly, the intense absorption band extending from 800 to 1200 cm^{-1} (peaks at 856, 915, and 1175 cm^{-1}) ascribe to a vaterite-type borate. The peak at 1346 cm^{-1} is asymmetric stretching of the BO_3 group. A small peak near 571 cm^{-1} can be distinguished as an in-plane blending of the BO_4 group or the BO_3 group in vaterite-type borates. This is in good accordance with the XRD result above. The peaks of 3433 and 1629 cm^{-1} are ascribed to the OH stretching vibration mode and the HOH bending vibration mode of the H_2O molecule, respectively. The reason for the existence of water is that residual water in the sample and the sample absorbing moisture during the IR measurement. For precise estimation of the proportion of water in the sample, we carried out a TG analysis as shown in Fig. 2b. The weight loss of 2.8% before 500 °C is due to the evaporation of weakly bonded

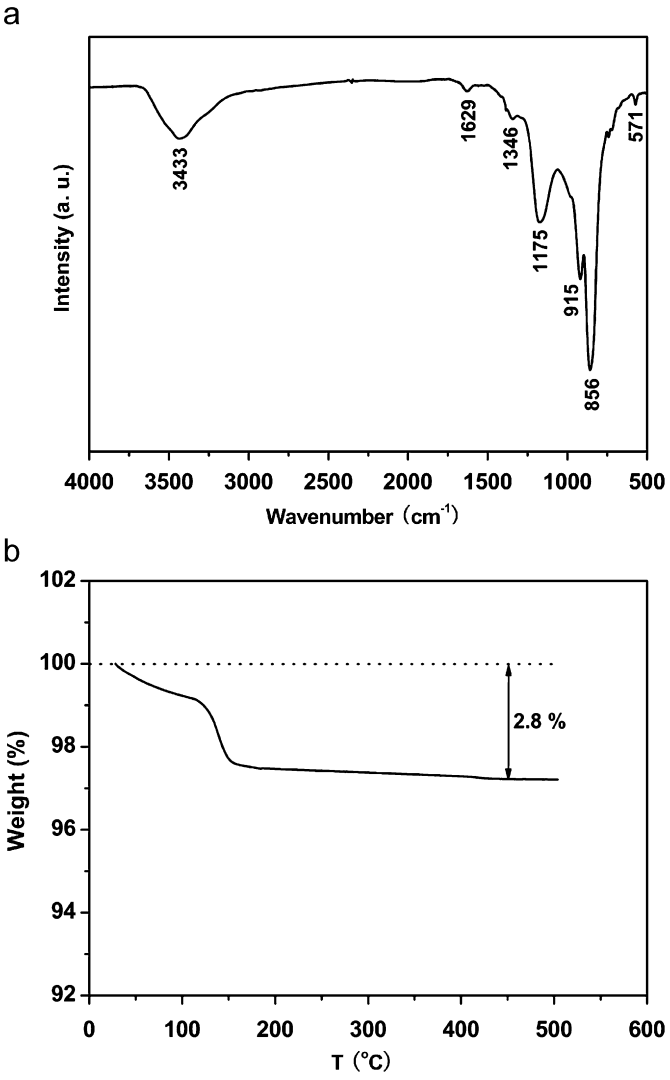

Fig. 2. IR spectrum (a) and TGA curve (b) of the $LuBO_3$:15%Tb^{3+} sample.

molecules, i.e., residual water molecules attached on the particle surface in the sample [10b]. Generally, most phosphors prepared from wet chemistry methods crystallize and exhibit luminescence only after being sintered at high temperature. In our present work, we do not further calcine the hydrothermal products at high temperature for two reasons: (1) the $LuBO_3$:Tb^{3+} obtained through the hydrothermal process is with high crystallinity (Fig. 1) and its PL luminescence intensity reaches 88% of that of the sample obtained from SR (Fig. 7); (2) Tb^{3+} will be oxidized easily at higher temperatures in the atmosphere. This is also the merit of our present reported process for $LuBO_3$:Tb^{3+} phosphors. The $LuBO_3$:Tb^{3+} is a good example to show that hydrothermal synthesis (wet chemistry processes) is also a fine way to prepare desired rare earth (RE) ions doped phosphors, without further sintering at higher temperatures.

3.2. Morphology and structure

The SEM images of the $LuBO_3$:15%Tb^{3+} sample are shown in Fig. 3a–c, which show that the sample consists of microflowers with a diameter of about 14 μm, each of which is constructed by densely packed nanoflakes with a thickness of about 40 nm and smooth surfaces. Because smaller nanograins contribute more to the broadening of the diffraction peaks, the average nanocrystal

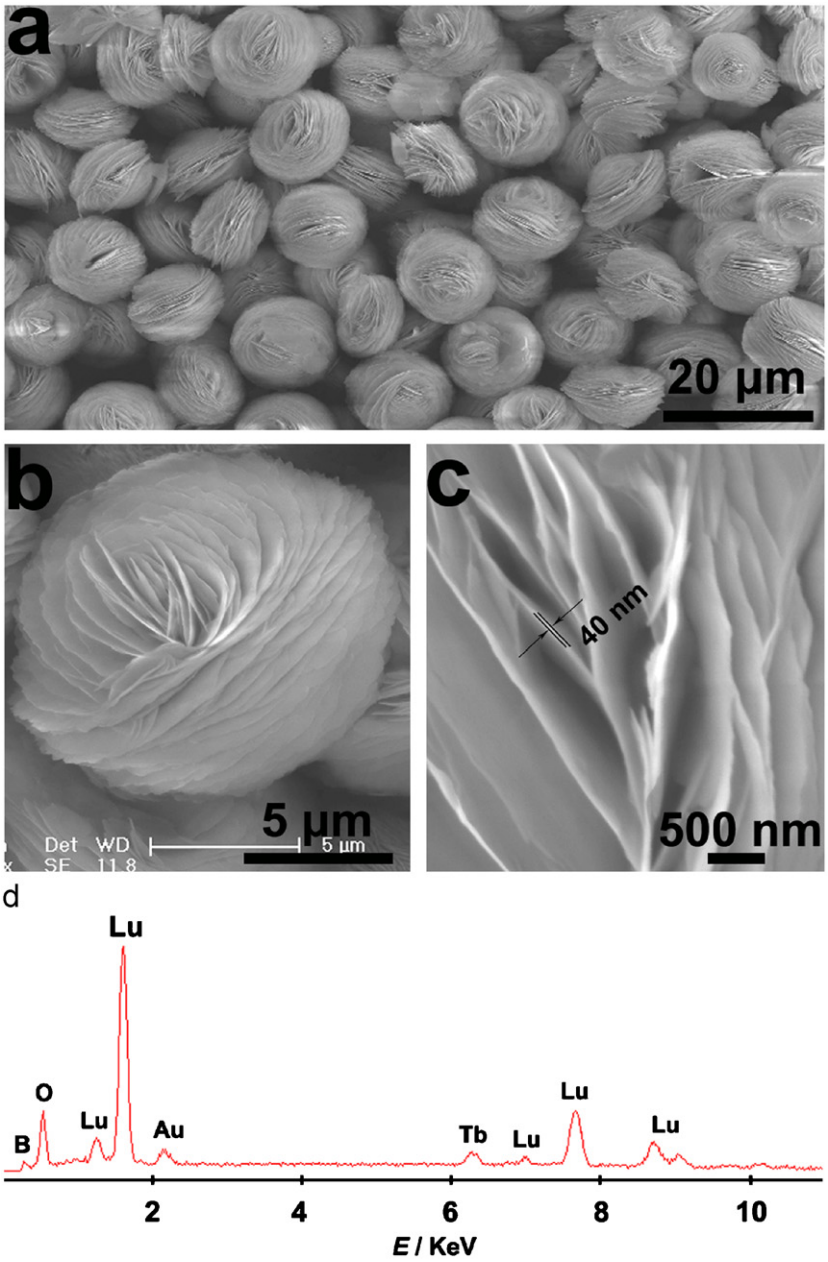

Fig. 3. SEM images of the $LuBO_3$:15%Tb^{3+} sample (a–c), EDX spectrum of $LuBO_3$:15%Tb^{3+} (d). Here, the Au signal is due to the Au coating for measurement.

size estimated from the Scherrer equation is smaller than that determined from SEM topology in the case of $LuBO_3$:15%Tb^{3+} microflowers [10c]. Detailed surface observation (Fig. 3b, c) implies that these microarchitectures are loosely and highly porous, and most of the nanoflakes are linked together by both edge-to-edge and edge-to-surface conjunctions; the nanoflakes extend outward from the center of the microstructure, and a few of them attach to each other. Therefore, such an architecture is a result of some type of self-assembly [1c,11]. The EDX was used to further characterize the composition of the as-prepared product. The EDX spectrum (Fig. 3d) of the $LuBO_3$:15%Tb^{3+} sample shows the presence of Lu, O, B and Tb, which matches well with $LuBO_3$ and Tb^{3+} has been effectively built into the $LuBO_3$ host lattice, agreeing with the XRD analysis above.

To further study the fine structure of the above microflowers, TEM was performed. Fig. 4a shows a broken flake of the flower obtained by ultrasonic treatment for about 30 min. These nanoflakes are several hundred nanometers in the planar dimensions with smooth surfaces. The corresponding SAED pattern of the broken nanoflake taken along the [001] zone axis shown in Fig. 4b reveals that the nanoflake ED pattern is characteristic of a hexagonal $LuBO_3$:Tb^{3+}, in good accordance with the XRD result. Moreover, SAED patterns, taken from both different areas on a single fragment and different fragments, were found to be identical within experimental accuracy, indicating that the $LuBO_3$:Tb^{3+} nanoflakes are single-crystalline and that different nanoflakes have identical crystallization habits. The patterns also reveal that the nanoflakes are stable enough to withstand the irradiation of convergent high-energy electron beams. Fig. 4c is a high-resolution TEM image of the $LuBO_3$:15%Tb^{3+} nanoflakes, which was taken with an electron beam along the [001] zone axis, perpendicular to the wide surface of the flake. The lattice fringes show the imaging characteristics of the hexagonal $LuBO_3$ crystal, in which the *d* spacing of 0.323 nm corresponds to the distance of the (100) planes. Further analysis indicates that the $LuBO_3$:Tb^{3+} nanoflake grows along the [100] or [010] crystallographic

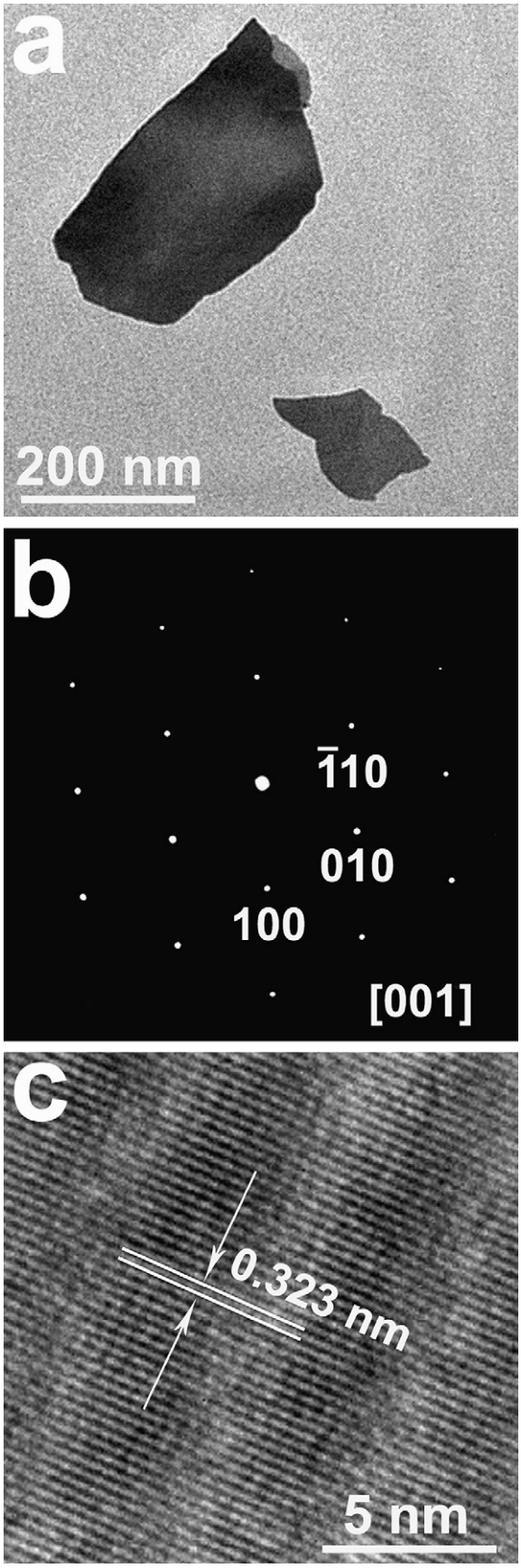

Fig. 4. Representative TEM image of the $LuBO_3$:15%Tb^{3+} nanoflake shed from the microflowers after ultrasonic treatment for 30 min (a), the corresponding electron diffraction pattern (b) and HRTEM image of the broken nanoflake shown in part a (c).

direction and is enclosed by $\pm(001)$ facets [12], i.e., the widest facets, as suggested in the XRD measurement.

Enlightened by our experimental results and the previous reports [1c,9a,c,d,13], we explain the synthesis reaction for the $LuBO_3$ phase under hydrothermal condition simply as follows:

$$Lu^{3+} + H_xBO_3^{(3-x)-} \rightarrow LuBO_3 + xH^+ \quad (x = 0, 1, 2, 3) \qquad (2)$$

The excess amount of H_3BO_3 and high pH value would accelerate the reaction toward the right to form $LuBO_3$, which can be proved by the fact that an increasing amount of H_3BO_3 or pH value leads to more products being obtained under the same reaction conditions. Since lutecium exists in the form of amorphous precipitates, the dissolution of the precipitates should occur firstly, to produce Lu^{3+}. H_3BO_3 could exist in a different form because it can be ionized further under hydrothermal condition, even though it is a weak acid. The reaction above is controlled by the dissolution of the amorphous precipitates and the precipitation of $LuBO_3$ (dissolution/precipitation), which is a common mechanism in hydrothermal synthesis.

Although the exact mechanism for the formation of these flowers is still unclear, it is believed that the growth of the flowerlike morphology is not assisted by a catalyst or directed by a template. In the present experiment, the dissolution of the amorphous precipitates should occur firstly, which precipitated to become the nuclei and quickly grew into nanoflakes due to the natural growing habit of forming a flakelike morphology (2D structure) along the *a*- and *b*-axis with a highly anisotropic structure during the growth process of rare earth orthoborates [9a,b,d,13]. In the following secondary growth stage, other tiny nanoflakes extend at an angle to the plane of the first flake from the center to form primary microflowers at the expense of the amorphous precipitates and/or small crystals. The primary microflowers continued to grow in a homocentric layer-by-layer growth style [14] and hierarchical flowerlike structures are formed to reduce the surface energy. A possible schematic illustration of the formation mechanism of this flowerlike structure is shown in Scheme 1. In this formation process, the reaction time was the most important controlling factor. Such a process is consistent with previous reports of a so-called two-stage growth process, which involves a fast nucleation of amorphous primary particles followed by a slow aggregation and crystallization of primary particles [15]. The bigger particles grew at the cost of the smaller ones, because there is different solubility between relatively

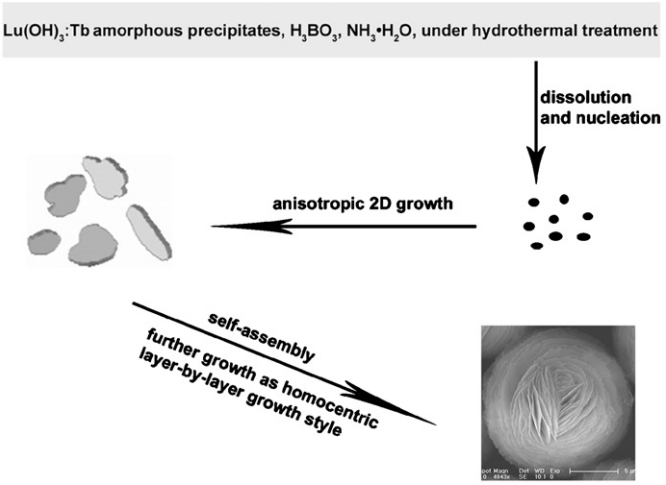

Scheme 1. The morphological evolution process of the $LuBO_3$:Tb^{3+} flowerlike structure.

larger and smaller particles according to the Gibbs–Thomson law [16]. The surface of the petals in the flowerlike structure is very smooth, probably due to Ostwald ripening [15a]. The boundaries of these flowers are composed of the thin edges of many flakes. The area of point contacts between adjacent flowers is therefore small. This minimizes the interaction between these flowers, so that they do not agglomerate. This is an advantage when suspensions are used for fabricating devices where coating uniformity is important. The mechanism for the formation of the final structure morphology by interaction between primary particles remains a mystery to materials chemists [15b], although many kinds of flowerlike 3D structures have been reported [11,14,15c,17]. Several factors, including crystal-face attraction, electrostatic and dipolar fields associated with the aggregate, van der Waals forces, hydrophobic interactions and hydrogen bonds, may have various effects on the self-assembly [15c,18].

3.3. Photoluminescence properties

The $LuBO_3$:Tb^{3+} sample emits bright-green light under UV excitation. Fig. 5 shows the excitation (a) and emission (b) spectra of the $LuBO_3$:15%Tb^{3+}sample. The excitation spectrum of $LuBO_3$:15%Tb^{3+} (Fig. 5a) monitored with 542 nm emission of Tb^{3+} ($^5D_4 \rightarrow {}^7F_5$) consists of two bands with maximum at 248 and 288 nm in the range of 200–300 nm in the UV excitation spectrum due to the f–d transitions of Tb^{3+} in the $LuBO_3$ lattice. The ground states ($4f^8$) of the Tb^{3+} are ^7F_J configurations; when one electron is promoted to the 5d shell, it gives rise to two $4f^7 5d^1$ excitation states: the high-spin state with ^9D_J configurations or the low-spin state with ^7D_J configurations. Obviously, ^9D_J states will be lower in energy according to Hund's rule, and the transitions between ^7F_J and ^7D_J are spin-allowed, while the transitions between ^7F_J and ^9D_J are spin-forbidden. Therefore, Tb^{3+} in a specific host exhibits two groups of f–d transitions: the spin-allowed $4f^8 \rightarrow 4f^7 5d^1$ ($^7F_6 \rightarrow {}^7D$) transition with higher energy (248 nm, $\Delta S = 0$) and the spin-forbidden $4f^8 \rightarrow 4f^7 5d^1$ ($^7F_6 \rightarrow {}^9D$) transition with lower energy (288 nm, $\Delta S = 1$) of the Tb^{3+} ion, respectively [19]. In the longer wavelength region, the f–f transition lines of Tb^{3+} can be observed with a weak intensity with respect to the f–d transitions of Tb^{3+} (inset in Fig. 5a), which are assigned as the transitions from the $^7F_6$ ground state to the different excited states of Tb^{3+}, i.e., 306 nm ($^5H_6$), 321 nm ($^5D_0$), 356 nm ($^5D_2$), 363 nm ($^5L_{10}$), 376 nm ($^5G_6$), 381 nm ($^5D_3$) and 489 nm ($^5D_4$), respectively [20]. Note that the $\Delta S = 1$ component is 5600 cm^{-1} below the $\Delta S = 0$ component for the Tb^{3+} $4f^8 \rightarrow 4f^7 5d^1$ transitions, basically agreeing with the literature values (5800–6000 cm^{-1}) in the oxide host lattices [19d,e]. Upon excitation into the $4f^8 \rightarrow 4f^7 5d^1$ transition at 248 nm (or 288 nm), the obtained emission spectrum (Fig. 5b) of $LuBO_3$:15%Tb^{3+} consists of $f \rightarrow f$ transition lines within $4f^8$ electron configuration of Tb^{3+}, i.e., $^5D_4 \rightarrow {}^7F_6$ (488 nm) in the blue region and $^5D_4 \rightarrow {}^7F_5$ (542 nm) in the green region, as well as $^5D_4 \rightarrow {}^7F_4$ (591 nm) and $^5D_4 \rightarrow {}^7F_3$ (625 nm) in the red region. The strongest one is located at 542 nm, corresponding to the $^5D_4 \rightarrow {}^7F_5$ transition of Tb^{3+}. The luminescence provides us additional proof that the as-formed products are not a mixture of $LnBO_3$ (Ln = Lu, Tb), but that the Tb^{3+} ions have successfully entered the host crystal lattice as an activator under the hydrothermal process.

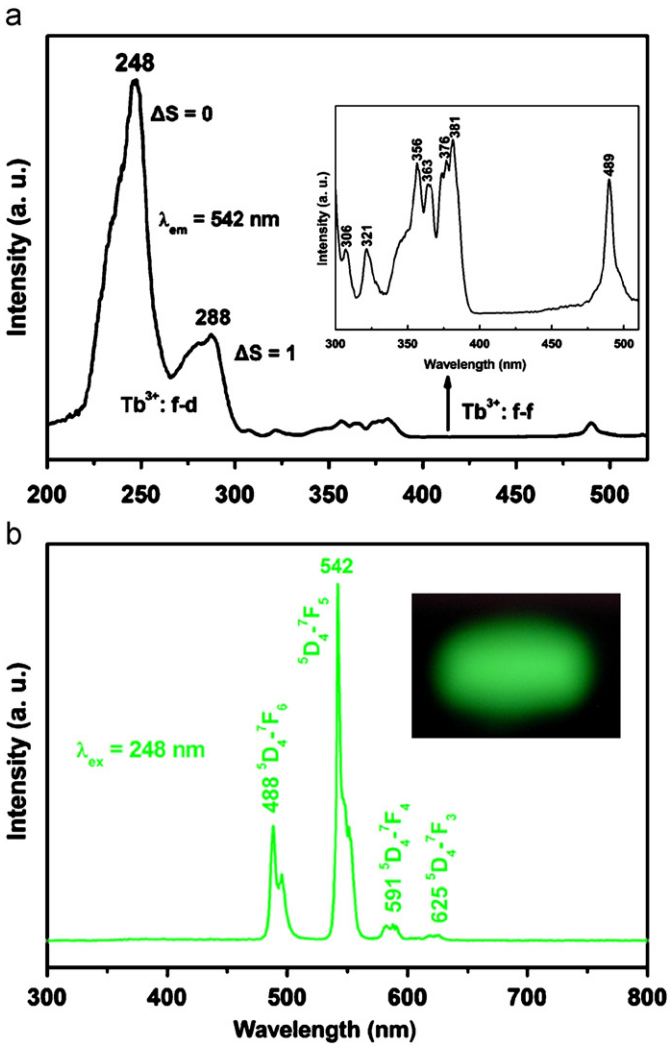

Fig. 5. Excitation (a) and emission (b) spectra of the $LuBO_3$:15%Tb^{3+}, respectively. Inset in part a is f–f transition lines of Tb^{3+} in the $LuBO_3$:15%Tb^{3+} sample. Inset in part b is the photograph of the photoluminescence color for the $LuBO_3$:15%Tb^{3+} sample under a 254-nm ultraviolet lamp excitation in dark room.

The decay curve (Fig. 6) for the luminescence of Tb^{3+} (monitored by $^5D_4 \rightarrow {}^7F_5$, 542 nm) can be well fitted into single exponential function,

$$I_{(t)} = I_0 \exp(-t/\tau) \quad (3)$$

where I_0 is the initial emission intensity at $t = 0$, and τ is the $1/e$ lifetime of the emission center. And the lifetime τ for the $^5D_4$ state of Tb^{3+} is determined to be 4.31 ms in the $LuBO_3$:15%Tb^{3+} sample obtained by the hydrothermal process (Fig. 6a), in the range of milliseconds due to the forbidden nature of the f–f transition [21a,b]. This value is a little longer than the lifetime obtained for the $LuBO_3$:15%Tb^{3+} sample (3.50 ms) prepared by solid-state reaction (Fig. 6b). The different luminescence lifetimes might be due to the different kinds and amounts of defects/impurities incorporated into the samples prepared by different methods [8e,21c,d]. The CIE chromaticity coordinates of the as-prepared $LuBO_3$:15%Tb^{3+} sample are $x = 0.2619$ and $y = 0.6123$, which is near to the NTSC Green [21e].

By varying the contents of Tb^{3+} ion in $LuBO_3$, we determined the optimum compositions with the highest emission intensity. In the emission spectra, the line positions and line width did not change as the Tb^{3+} concentration changed, indicating the nature of the Tb^{3+} activation did not change with concentration. On the other hand, the PL intensities changed with Tb^{3+} concentration. Fig. 7a shows the dependence of the PL emission intensity of Tb^{3+} (integrated intensity of $^5D_4 \rightarrow {}^7F_{6,\,5,\,4,\,3}$) on its doping concentration in $LuBO_3$ flowers. It was found that the PL emission intensity increased firstly and then decreased. The results showed that the optimum dopant concentration for Tb^{3+} is 15% of Lu^{3+} in the $LuBO_3$ host (Fig. 7a) and here the PL luminescence intensity reaches 88% of that of the sample obtained from SR (Fig. 7b).

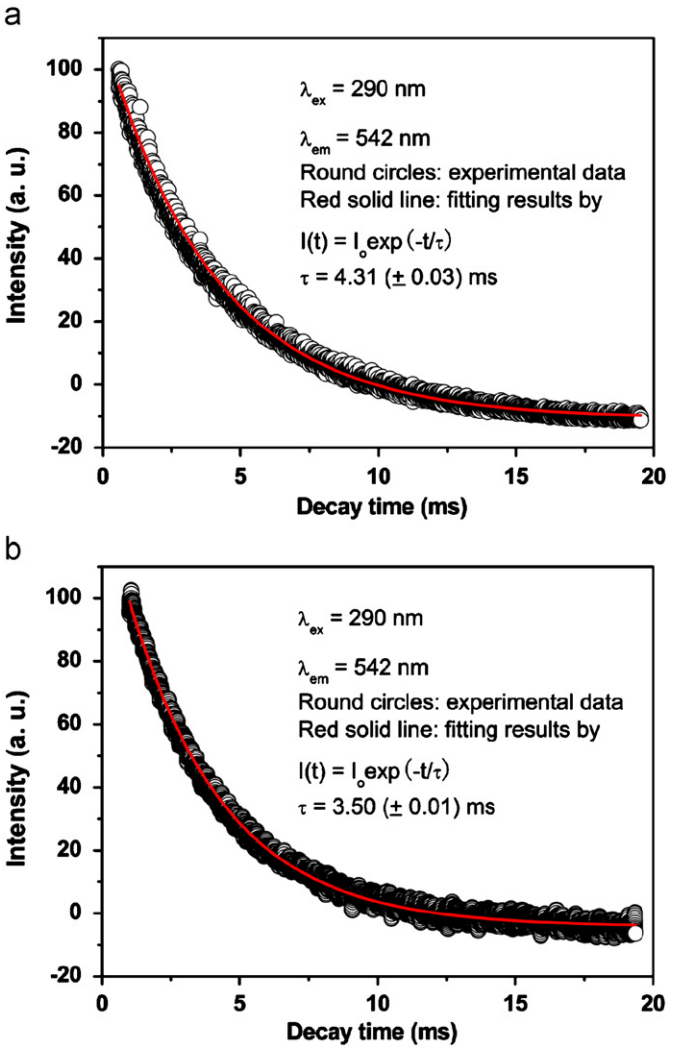

Fig. 6. The decay curves for the luminescence of Tb^{3+} in $LuBO_3$:15%Tb^{3+} prepared by the hydrothermal process (a) and solid-state reaction (b).

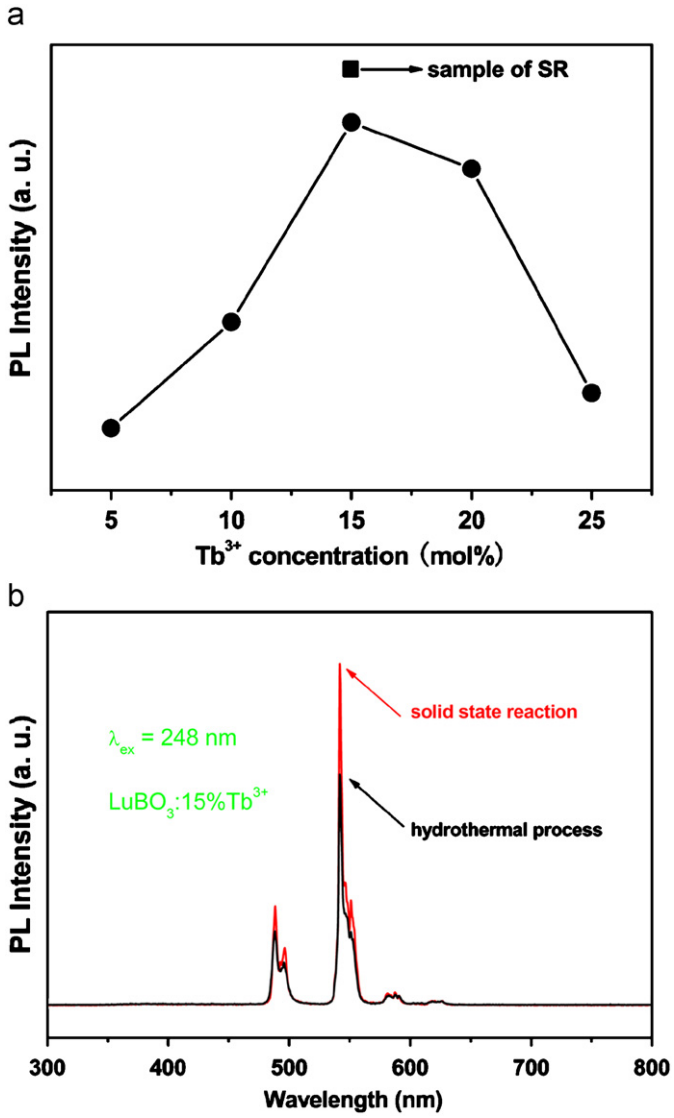

Fig. 7. The photoluminescence emission intensity (integrated intensity of $^5D_4 \rightarrow {}^7F_{6,\ 5,\ 4,\ 3}$) of Tb^{3+} ions as a function of its doping concentration in the $LuBO_3$ host (a). The emission intensity of the $LuBO_3$:15%Tb^{3+} sample obtained from SR is also presented in the figure for comparison. The emission spectra of $LuBO_3$:15%Tb^{3+} synthesized by SR (b).

(The emission spectrum of $LuBO_3$:15%Tb^{3+} synthesized by SR is basically similar to that of $LuBO_3$:Tb^{3+} obtained through the hydrothermal process due to the excitation and emission of Ln^{3+} arising from *f–f* transitions, which are strongly shielded by the outside 5*s* and 5*p* electrons.) The decrease of PL emission intensity for concentrations greater than the optimum dopant concentration (15%) might be caused by the concentration quenching effect, which was caused by the cross-relaxation between neighboring Tb^{3+} ions. Considering that luminescence quenching is caused by the energy transfer within the same rare earth ions, the critical distance (R_C) can be estimated in terms of the equation

$$R_C = 2(3V/4\pi N X_C)^{1/3} \quad (4)$$

where V is the volume of the unit cell, X_C is the critical concentration and N is the number of available crystallographic sites occupied by the activator ions in the unit cell [22]. The values of V and N for the crystalline $LuBO_3$ (hexagonal system, $Z = 2$, $V = a^2c \sin 120^\circ$, $N = Z$) are 0.1049 nm^3 and 2, respectively (JCPDS card 74-1938). Considering the above optimum concentration as the critical concentration X_C, the R_C for Tb^{3+} is 0.874 nm in the crystalline $LuBO_3$ host.

In addition, the typical non-linear variation of the PL intensity provides further evidence that our sample consists of doped particles and not of a mixture of $TbBO_3$ and $LuBO_3$ particles. In the latter case the PL intensity is expected to increase steadily with increasing the rare earth ion (Tb^{3+}) concentration [23].

3.4. Cathodoluminescence properties

Under low-voltage electron beams excitation, the as-prepared vaterite-type $LuBO_3$:Tb^{3+} particles exhibit a strong green emission. The typical cathodoluminescence emission spectrum of $LuBO_3$:15%Tb^{3+} phosphors under the excitation of electron beams (accelerating voltage = 4 kV; filament current = 102 mA) are shown in Fig. 8a, which are similar to the corresponding PL emission spectrum shown in Fig. 5b. The CL emission intensities for $LuBO_3$:15%Tb^{3+} phosphors has been investigated as a function of the accelerating voltage and the filament current, as shown in Fig. 8b and c, respectively. When the filament current is fixed at 102 mA, the CL intensity increased with increasing the accelerating voltage from 3 to 5 kV (Fig. 8b). Similarly, under a 4 kV electron beams excitation, the CL intensity also increases with increasing the filament current from 93 to 105 mA (Fig. 8c).

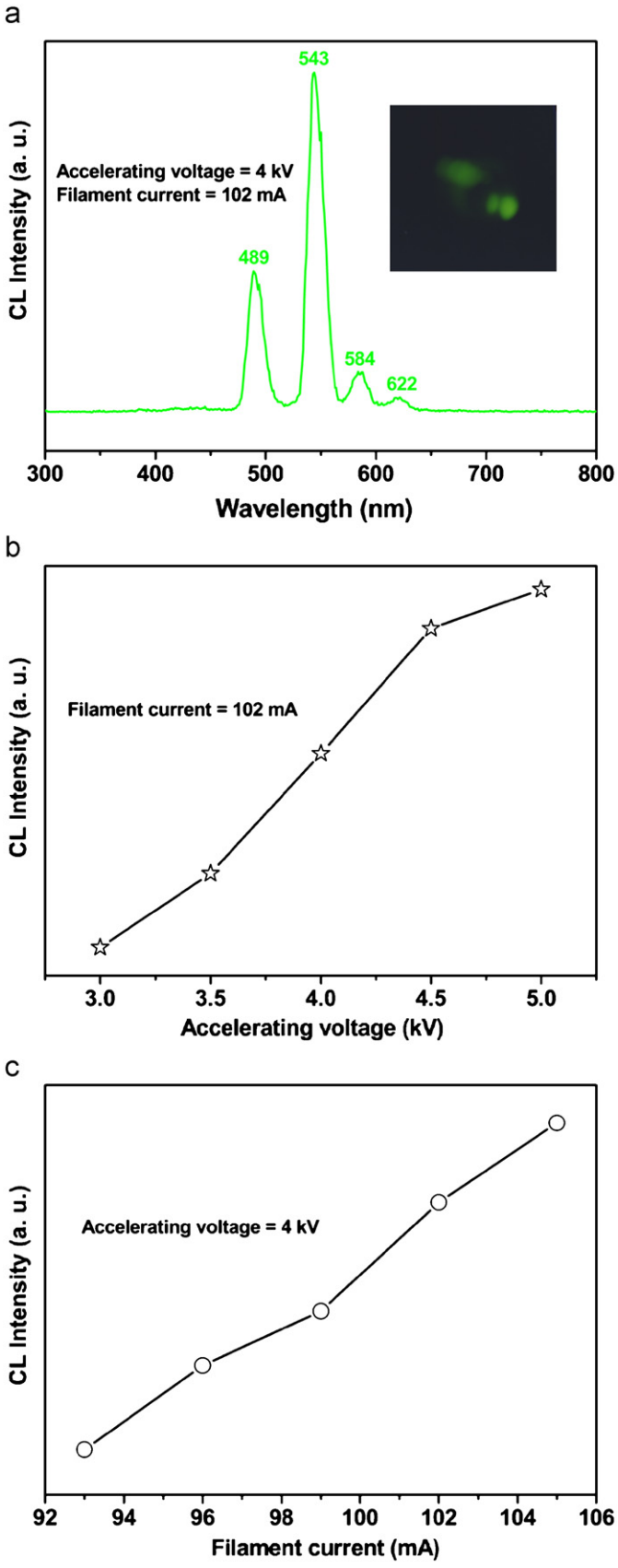

Fig. 8. Typical cathodoluminescence spectrum of the $LuBO_3$:15%Tb^{3+} sample (a) (accelerating voltage = 4 kV; filament current = 102 mA), and the CL intensity of the $LuBO_3$:15%Tb^{3+} sample as a function of accelerating voltage (b) and filament current (c), respectively. Inset in part a is the photograph of the cathodoluminescence color for the $LuBO_3$:15%Tb^{3+} sample under accelerating voltage = 4 kV and filament current = 102 mA in dark room.

For cathodoluminescence, the Tb^{3+} ions are excited by the plasma produced by the incident electrons. The electron penetration depth can be estimated by

$$L[\text{Å}] = 250(A/\rho)(E/Z^{1/2})^n \quad (5)$$

where $n = 1.2/(1-0.29\log_{10}Z)$, A is the atomic or molecular weight of the material, ρ is the bulk density, Z is the atomic number or the number of electrons per molecule in the case compounds, and E is the accelerating voltage (kV) [24]. For hexagonal vaterite-type $LuBO_3$:Tb^{3+}, the calculated electron penetration depth at 3 kV is 26.2 nm. This value is within the $LuBO_3$:Tb^{3+} flake thickness (Fig. 3c). With the increase in accelerating voltage, more plasma will be produced by the incident electrons, resulting in more Tb^{3+} being excited and higher CL intensity. The increase in electron energy is attributed to the deeper penetration of electrons into the phosphor body, which is governed by Eq. (5). The deeper penetration of electrons in the phosphor body results in an increase in electron–solid interaction volume in which the excitation of Tb^{3+} ions is responsible for light emission. Therefore, an increase in interaction volume (which effectively determines the generation of light inside the phosphor) with an increase in electron energy brings about an increase in the CL brightness of $LuBO_3$:Tb^{3+} particles [25]. Due to the strong low-voltage CL intensity of $LuBO_3$:Tb^{3+} phosphors, they may find possible applications in field emission display devices.

4. Conclusions

In summary, we have demonstrated a simple and mild hydrothermal method for synthesis of the fine, dispersed and homogeneous $LuBO_3$:Tb^{3+} microflower phosphors directly without further sintering treatment and reductive ambience for protection. This simple synthetic method, which does not use any surfactant or template, may be extended to the synthesis of other materials with novel 3D morphologies. The morphology, microstructure, crystal structure, chemical composition, and optical properties were characterized by XRD, FT-IR, TGA, SEM, EDX, TEM, HRTEM, SAED, PL, CL, and kinetic decays. The reaction mechanism has been considered as a dissolution/precipitation mechanism; the self-assembly evolution process has been proposed on a homocentric layer-by-layer growth style. Due to the strong green emission corresponding to $^5D_4 \rightarrow {}^7F_5$ (542 nm) of Tb^{3+} under ultraviolet excitation and low-voltage electron beams excitation and excellent dispersing properties, the as-formed $LuBO_3$:Tb^{3+} microflower phosphors are potentially applied in fluorescent lamps and field emission displays.

Acknowledgments

This project was financially supported by the foundation of "Bairen Jihua" of Chinese Academy of Sciences, the MOST of China (Nos. 2003CB314707 and 2007CB935502) and the National Natural Science Foundation of China (50572103, 20431030 and 00610227).

References

[1] (a) C. Lind, A.P. Wilkinson, C.J. Rawn, E.A. Payzant, J. Mater. Chem. 11 (2001) 3354;
(b) J. Yang, X.M. Liu, C.X. Li, Z.W. Quan, D.Y. Kong, J. Lin, J. Cryst. Growth 303 (2007) 480;
(c) J. Yang, C.X. Li, X.M. Zhang, Z.W. Quan, C.M. Zhang, H.Y. Li, J. Lin, Chem. Eur. J. 14 (2008) 4336;
(d) A. Huignard, T. Gacoin, J.P. Boilot, Chem. Mater. 12 (2002) 1090.
[2] (a) Y.X. Pan, M.M. Wu, Q. Su, Mater. Res. Bull. 38 (2003) 1537;
(b) T.R.N. Kutty, M. Nayak, Mater. Chem. Phys. 65 (2000) 158.

[3] (a) M. Ren, J.H. Lin, Y. Dong, L.Q. Yong, M.Z. Su, L.P. You, Chem. Mater. 11 (1999) 1576;
(b) G. Bertrand-Chadeyron, R. Mahiou, M. El-Ghozzi, A. Arbus, D. Zambon, J.C. Cousseins, J. Lumin. 72–74 (1997) 564;
(c) L. Lou, D. Boyer, G. Chadeyron, E. Bernstein, R. Mahiou, J. Mugnier, Opt. Mater. 15 (2000) 1.
[4] (a) Z.H. Li, J.H. Zeng, C. Chen, Y.D. Li, J. Cryst. Growth 286 (2006) 487;
(b) K.N. Kim, H.K. Jung, H.D. Park, J. Mater. Res. 17 (2002) 907;
(c) G. Bertrand-Chadeyron, M. El-Ghozzi, D. Boyer, R. Mahiou, J.C. Cousseins, J. Alloys Compd. 317–318 (2001) 183;
(d) D. Boyer, G. Bertrand-Chadeyron, R. Mahiou, C. Caperaa, J.C. Cousseins, J. Mater. Chem. 9 (1999) 211.
[5] (a) O. Guillot-Noël, B. Bellamy, B. Viana, D. Vivien, Phys. Rev. B 60 (1999) 1668;
(b) B. Moine, C. Dujardin, H. Lautesse, C. Pedrini, C.M. Combes, A. Belski, P. Martin, J.Y. Gesland, Mater. Sci. Forum 239–241 (1997) 245;
(c) J.A. Capobianco, F. Vetrone, J.C. Boyer, A. Speghini, M. Bettinelli, Opt. Mater. 19 (2002) 259.
[6] (a) L. Zhang, C. Pedrini, C. Madej, C. Dujardin, J.C. Gâcon, B. Moine, I. Kamenskikh, A. Belsky, D.A. Shaw, M.A. MacDonald, P. Mesnard, C. Fouassier, J.C. Van't Spijker, C.W.E. Van Eijk, Radiat. Eff. Defects Solids 150 (1999) 439;
(b) M. Balcerzyk, Z. Gontarz, M. Moszynski, M. Kapusta, J. Lumin. 87–89 (2000) 963.
[7] (a) C. Mansuy, J.M. Nedelec, C. Dujardin, R. Mahiou, Opt. Mater. 29 (2007) 697;
(b) D. Boyer, G. Bertrand-Chadeyron, R. Mahiou, L. Lou, A. Brioude, J. Mugnier, Opt. Mater. 16 (2001) 21;
(c) J. Hälsö, Inorg. Chim. Acta 139 (1987) 257.
[8] (a) C. Serre, N. Stock, T. Bein, Inorg. Chem. 43 (2004) 3159;
(b) X. Wang, Y.D. Li, Angew. Chem. Int. Ed. 42 (2003) 3497;
(c) C.J. Jia, L.D. Sun, L.P. You, X.C. Jiang, F. Luo, Y.C. Pang, C.H. Yan, J. Phys. Chem. B 109 (2005) 3284;
(d) J. Yang, C.K. Lin, Z.L. Wang, J. Lin, Inorg. Chem. 45 (2006) 8973;
(e) J. Yang, Z.W. Quan, D.Y. Kong, X.M. Liu, J. Lin, Cryst. Growth Des. 7 (2007) 730.
[9] (a) X.C. Jiang, L.D. Sun, C.H. Yan, J. Phys. Chem. B 108 (2004) 3387;
(b) J. Zhang, J. Lin, J. Cryst. Growth 271 (2004) 207;
(c) Z.H. Li, J.H. Zeng, Y.D. Li, Small 3 (2007) 438;
(d) X.C. Jiang, L.D. Sun, W. Feng, C.H. Yan, Cryst. Growth Des. 4 (2004) 517;
(e) Y.H. Wang, K. Uheda, H. Takizawa, T. Endo, Chem. Lett. 3 (2001) 206;
(f) X.C. Jiang, C.H. Yan, L.D. Sun, Z.G. Wei, C.S. Liao, J. Solid State Chem. 175 (2003) 245;
(g) J. Ma, Q.S. Wu, Y.P. Ding, Y. Chen, Cryst. Growth Des. 7 (2007) 1553.
[10] (a) L. Guerbous, O. Krachni, Radiat. Eff. Defects Solids 161 (2006) 199;
(b) D. Boyer, F. Leroux, G. Bertrand, R. Mahiou, J. Non-Cryst. Solids 306 (2002) 110;
(c) Y.W. Zhang, S. Jin, S.J. Tian, G.B. Li, T. Jia, C.S. Liao, C.H. Yan, Chem. Mater. 13 (2001) 372;
(d) Y.H. Wang, C.F. Wu, J.C. Zhang, Mater. Res. Bull. 41 (2006) 1571.
[11] W.B. Bu, Y.P. Xu, D.Y. Jiang, J.L. Shi, J. Phys. Chem. C 111 (2007) 5014.
[12] J.Q. Hu, Y. Bando, J.H. Zhan, Y.B. Li, T. Sekiguchi, Appl. Phys. Lett. 83 (2003) 4414.
[13] T. Kim, S. Kang, Mater. Res. Bull. 40 (2005) 1945.
[14] L.X. Yang, Y.J. Zhu, L. Li, L. Zhang, H. Tong, W.W. Wang, G.F. Cheng, J.F. Zhu, Eur. J. Inorg. Chem. (2006) 4787.
[15] (a) Y. Cheng, Y.S. Wang, Y.H. Zheng, Y. Qin, J. Phys. Chem. B 109 (2005) 11548;
(b) J. Park, V. Privman, E. Matijevic, J. Phys. Chem. B 105 (2001) 11630;
(c) L.S. Zhong, J.S. Hu, H.P. Liang, A.M. Cao, W.G. Song, L.J. Wan, Adv. Mater. 18 (2006) 2426.
[16] J.W. Mullin (Ed.), Crystallization, 3rd ed, Butterworth-Heinemaan, Oxford, 1997.
[17] (a) A.C. Chen, X.S. Peng, K. Koczkur, B. Miller, Chem. Commun. (2004) 1964;
(b) Y.P. Zhao, D.X. Ye, G.C. Wang, T.M. Lu, Nano Lett. 2 (2002) 351;
(c) X.S. Fang, C.H. Ye, L.D. Zhang, J.X. Zhang, J.W. Zhao, P. Yan, Small 1 (2005) 422;
(d) Y.B. Li, Y. Bando, D. Golberg, Appl. Phys. Lett. 82 (2003) 1962.
[18] (a) Y. Politi, T. Arad, E. Klein, S. Weiner, L. Addadi, Science 306 (2004) 1161;
(b) H. Colfen, M. Antonietti, Angew. Chem. Int. Ed. 44 (2005) 5576;
(c) H. Colfen, S. Mann, Angew. Chem. Int. Ed. 42 (2003) 2350.
[19] (a) W. Chen, R. Sammynaiken, Y. Huang, J. Appl. Phys. 88 (2000) 1424;
(b) E. Zych, Opt. Mater. 16 (2001) 445;
(c) E. Zycha, J. Trojan-Piegza, D. Hreniak, W. Strek, J. Appl. Phys. 94 (2003) 1318;
(d) J. Lin, Q. Su, J. Mater. Chem. 5 (1995) 1151;
(e) G. Blasse, A. Bril, Philips Res. Rep. 22 (1967) 481.
[20] K.S. Thomas, S. Singh, G.H. Dieke, J. Chem. Phys. 38 (1963) 2180.
[21] (a) M. Yu, H. Wang, C.K. Lin, G.Z. Li, J. Lin, Nanotechnology 17 (2006) 3245;
(b) Z.L. Wang, Z.W. Quan, P.Y. Jia, C.K. Lin, Y. Luo, Y. Chen, J. Fang, W. Zhou, C.J. O'Connor, J. Lin Chem. Mater. 18 (2006) 2030;
(c) H. Wang, C.K. Lin, X.M. Liu, J. Lin, Appl. Phys. Lett. 87 (2005) 181907;
(d) M.L. Pang, J. Lin, Z.Y. Cheng, Mater. Sci. Eng. B 100 (2003) 124;
(e) F.S. Kao, Mater. Chem. Phys. 76 (2002) 295.
[22] G. Blasse, Philips Res. Rep. 24 (1969) 131.
[23] M.L. Pang, J. Lin, J. Fu, R.B. Xing, C.X. Luo, Y.C. Han, Opt. Mater. 23 (2003) 547.
[24] C. Feldman, Phys. Rev. 117 (1960) 55.
[25] D. Kumar, K.G. Cho, Z. Chen, V. Craciun, P.H. Holloway, R.K. Singh, Phys. Rev. B 60 (1999) 13331.